

A multi-wavelength study of the 2025 low state of the intermediate polar BG CMi

A. W. SHAW ,¹ K. MUKAI ,^{2,3} C. O. HEINKE ,⁴ C. G. NIXON,¹ D. A. H. BUCKLEY ,^{5,6,7} P. A. DUBOVSKÝ ,^{8,9} F.-J. HAMBSCH ,^{10,11,12,13} J. HILBURN,¹⁴ K. PETRÍK,¹⁵ R. M. PLOTKIN ,^{16,17} S. B. POTTER ,^{5,18} N. RAWAT,⁵ T. SHAHBAZ ,^{19,20} S. DUFOER,^{10,13} S. DVORAK,^{10,21} D. MESSIER,^{10,22} G. MYERS,¹⁰ P. NELSON,^{10,23} R. SABO,^{10,24} J. ULOWETZ,^{10,25} AND T. VANMUNSTER^{10,26,27,13}

¹Department of Physics & Astronomy, Butler University, 4600 Sunset Avenue, Indianapolis, IN 46208, USA

²CRESST II and X-ray Astrophysics Laboratory, NASA/GSFC, Greenbelt, MD 20771, USA

³Department of Physics, University of Maryland, Baltimore County, 1000 Hilltop Circle, Baltimore, MD 21250, USA

⁴Department of Physics, University of Alberta, Edmonton, AB, T6G 2E1, Canada

⁵South African Astronomical Observatory, PO Box 9, Observatory, 7935, Cape Town, South Africa

⁶Department of Astronomy, University of Cape Town, Private Bag X3, Rondebosch 7701, South Africa

⁷Department of Physics, University of the Free State, PO Box 339, Bloemfontein 9300, South Africa

⁸Vihorlat Observatory in Humenné, Slovakia

⁹Variable Star Section, Slovak Astronomical Society

¹⁰American Association of Variable Star Observers, 185 Alewife Brook Parkway, Suite 410, Cambridge, MA 02138, USA

¹¹Groupe Européen d'Observations Stellaires (GEOS), 23 Parc de Levesville, 28300 Bailleau l'Évêque, France

¹²Bundesdeutsche Arbeitsgemeinschaft für Veränderliche Sterne (BAV), Munsterdamm 90, 12169 Berlin, Germany

¹³Vereniging Voor Sterrenkunde (VVS), Zeeweg 96, 8200 Brugge, Belgium

¹⁴Great Basin Observatory, Great Basin National Park, Baker, NV 89311

¹⁵Observatory and Planetarium M. R. Štefánik in Hlohovec, Slovakia

¹⁶Department of Physics, University of Nevada, Reno, NV 89557, USA

¹⁷Nevada Center for Astrophysics, University of Nevada, Las Vegas, NV 89154, USA

¹⁸Department of Physics, University of Johannesburg, PO Box 524, Auckland Park 2006, South Africa

¹⁹Instituto de Astrofísica de Canarias, E-38205 La Laguna, Tenerife, Spain

²⁰Departamento de Astrofísica, Universidad de La Laguna, E-38206 La Laguna, Tenerife, Spain

²¹Rollinghills Observatory, Clermont, FL 34711, USA

²²Center for Backyard Astrophysics, 35 Sergeants Way, Lisbon, CT 06351

²³Wild Cherry Observatory, Wild Cherry Road, Lockwood South, Victoria 3551, Australia

²⁴1344 Post Drive, Bozeman, MT 59715, USA

²⁵Center for Backyard Astrophysics, 855 Fair Ln, Northbrook, IL 60062, USA

²⁶CBA Belgium Observatory, Walhostraat 1A, B-3401 Landen, Belgium

²⁷CBA Extremadura Observatory, E-06340 Fregenal de la Sierra, Badajoz, Spain

(Received XXXX; Revised XXXX; Accepted XXXX)

Submitted to ApJ

ABSTRACT

We present multi-wavelength observations of the first recorded low state of the intermediate polar BG CMi. Optical monitoring of the source by members of the American Association of Variable Star Observers reveals a decrease of ~ 0.5 mag that lasted ~ 50 d in early 2025. During the low state the optical timing properties imply that BG CMi underwent a change in the accretion mode, as power at the spin frequency ω dramatically dropped. An *XMM-Newton* observation revealed a substantial decrease in intrinsic absorption and a slight increase in intrinsic X-ray luminosity, compared to archival *Suzaku* data. Timing analysis of the X-ray light curves shows that power shifted from the orbital frequency Ω (prominent in *Suzaku* data) to 2Ω in the low state *XMM-Newton* data, along with the strengthening of certain orbital sidebands. We suggest that BG CMi transitioned to disk-overflow accretion, where the

white dwarf accreted matter via both a disk and a stream, the latter becoming more dominant during the low state due to a decrease in the mass and size of the disk.

Keywords: Cataclysmic variable stars (203) — DQ Herculis stars (407) — Accretion (14) — Stellar accretion disks (1579) — White dwarf stars (1799)

1. INTRODUCTION

Intermediate Polars (IPs) are a class of accreting white dwarfs and a subclass of cataclysmic variables in which a white dwarf (WD) accretes matter from a (typically) main-sequence companion. In IPs, a partial accretion disk can form. However the magnetic field of the WD is strong enough ($B \gtrsim 10^6$ G) to disrupt the innermost portion of the disk, such that the innermost edge lies at the magnetospheric radius. Material at the innermost edge of the disk flows along the magnetic field lines onto the magnetic poles of the WD (see e.g. [J. Patterson 1994](#); [L. Ferrario et al. 2015, 2020](#), for reviews).

One of the key observational signatures of IPs is multi-wavelength periodic variability. Unlike in polars, another class of magnetic CV, the spin period of the WD (P_{spin}) and the binary orbital period (P_{orb}) are not synchronized in IPs. Consequently, the power spectra of IP light curves at optical, UV, and X-ray wavelengths are typically dominated by the WD spin frequency ($\omega = 1/P_{\text{spin}}$), the orbital frequency ($\Omega = 1/P_{\text{orb}}$) and the beat frequency ($\omega - \Omega$). IPs have also been known to exhibit variability at orbital sidebands such as $\omega + \Omega$ and $\omega - 2\Omega$ ([B. Warner 1986](#)).

The timing properties of IPs contain information about the accretion properties of the system. Though the standard picture of accretion in IPs is one of a partial disk that is truncated at the magnetospheric radius (the ‘disk-fed’ model), there is strong evidence that at least one IP, V2400 Oph, has accreted via a ‘stream-fed’ mode in which material travels along a stream toward the WD magnetosphere without forming a disk (see e.g. [D. A. H. Buckley et al. 1995, 1997](#); [C. Hellier & A. P. Beardmore 2002](#)). A third accretion mode known as ‘disk-overflow’ can be considered as a hybrid of stream- and disk-fed accretion modes, as both types are observed simultaneously ([C. Hellier 1993](#); [P. J. Armitage & M. Livio 1996, 1998](#)). IPs have shown evidence of switching between accretion modes, in fact V2400 Oph itself, despite being the canonical ‘diskless IP’, has exhibited signs of disk-overflow accretion ([A. Joshi et al. 2019](#)), while a recent study has revealed a much more complex accretion system than previously thought ([A. Langford et al. 2022](#)). The observational evidence for these changes in accretion modes lies in the power spectra of IP light curves.

[G. A. Wynn & A. R. King \(1992\)](#) and [L. Ferrario & D. T. Wickramasinghe \(1999\)](#) have shown that the strengths of the different peaks in IP power spectra can be used to determine the dominant accretion mode in the system. For example, a typical disk-fed IP will show strong variability on ω at optical/UV and X-ray wavelengths, owing to the presence of a Keplerian disk, the inner edge of which co-rotates with the WD. However, in the stream-fed regime, the power spectra start to become more complex. [L. Ferrario & D. T. Wickramasinghe \(1999\)](#) showed that, for diskless IPs, the X-ray light curves might show variability at ω , $\omega - \Omega$ and $2\omega - \Omega$, with the strength of the peaks in the power spectra varying with binary inclination, i . In the optical, the power spectrum of a diskless IP might show strong peaks at ω , $\omega - 2\Omega$ and $2(\omega - \Omega)$, depending on i , with the power spectrum of a model low-inclination system ($i \sim 20^\circ$) completely dominated by the $2(\omega - \Omega)$ beat.

Changes in IP accretion modes have been seen to be coincident with a decrease in a source’s optical flux. These so-called ‘low-states’ have been known to exist for a while (e.g. [P. Garnavich & P. Szkody 1988](#)), but have been relatively poorly studied until recently. The IP FO Aqr has exhibited three excursions to a low state since 2015, during which it transitioned from a disk-fed to a stream-fed or disk-overflow accretion mode ([M. R. Kennedy et al. 2017](#); [C. Littlefield et al. 2020](#), e.g.). [A. E. Covington et al. \(2022\)](#) found evidence for changing accretion geometry in two IPs during their low states. In DO Dra, accretion may even have completely stopped for a short period during its low state ([K. L. Hill et al. 2022](#)). It is becoming evident that IP low states and changes in accretion geometry are linked. However, to truly understand the accretion processes at work, one must take a multi-wavelength approach. Only one IP low state has been studied at X-ray energies (FO Aqr; [M. R. Kennedy et al. 2017](#)), revealing changes in the X-ray spectrum that were interpreted as a switch to a stream-fed geometry. X-ray observations allow us to study the shock close to the surface of the WD, while optical photons typically originate from the accretion disk, including the hotspot, as well as from the irradiated face of the secondary. Multi-wavelength

observations allow us to paint a more complete picture of the physical processes at work during a low state.

Here, we present only the second deep X-ray study of an IP low state, after FO Aqr (M. R. Kennedy et al. 2017). In this work, we use the practical definition of “low state” as defined by A. E. Covington et al. (2022), i.e. a sustained drop in optical flux of $\gtrsim 0.5$ mag from the average. However, we acknowledge that there could be many meaningful definitions of a low state (see e.g. P. Garnavich & P. Szkody 1988; M. R. Kennedy et al. 2017; C. Littlefield et al. 2020).

We performed observations of the IP BG CMi with *XMM-Newton* in March 2025 during a time when the optical flux had decreased significantly. The X-ray observations were performed simultaneously with optical observations in a number of wavebands. The paper is structured as follows: in Section 2 we detail the observations and data reduction, in Section 3 we present both spectral and temporal analysis of the data and finally we discuss our results and present conclusions in Sections 4 and 5, respectively.

1.1. BG CMi

BG Canis Minoris (BG CMi) was first reported as the X-ray source 3A 0729+103 and quickly associated with a newly discovered CV (I. M. McHardy et al. 1982), before being confirmed as an IP (I. M. McHardy et al. 1984). The WD has a spin period of $P_{\text{spin}} = 913.5$ s (C. Hellier 1997) which has been shown to spin up over many observing campaigns, though the rate of spin-up has slowed down (Y. G. Kim et al. 2005; M. Bonnardeau 2016; J. Patterson et al. 2020). The binary orbital period is $P_{\text{orb}} = 3.23$ h (M. Bonnardeau 2016) such that $P_{\text{spin}}/P_{\text{orb}} \sim 0.08$ and thus BG CMi is expected to have a partial accretion disk, assuming spin equilibrium (A. R. King & J.-P. Lasota 1991). In March 2025, BG CMi was reported to have entered a low state, with optical monitoring of the source noting an overall fading of ~ 0.5 magnitudes (C. Littlefield et al. 2025). Prior to this, no low states of the source had been reported.

2. OBSERVATIONS AND DATA REDUCTION

2.1. *XMM-Newton*

BG CMi was observed by *XMM-Newton* for a total of 31 ks on 2025 March 23 at 19:00 UTC. The European Photon Imaging Camera (EPIC) detectors, consisting of the EPIC-pn (L. Strüder et al. 2001) and the two EPIC-MOS (M. J. L. Turner et al. 2001) were all operated in Large Window mode, affording 47.7 ms time resolution in pn and 0.9 s time resolution in MOS. The EPIC instruments also utilized a thin optical blocking filter. The

optical/UV monitor (OM; K. O. Mason et al. 2001) provided simultaneous observations in the *V*-band and was operated in Fast mode, providing 0.5 s time resolution.

Data were reduced using the *XMM-Newton* Science Analysis System (SAS) v22.1.0. To reprocess the EPIC data we used `epproc` and `emproc` for pn and MOS, respectively. EPIC event lists were filtered for periods of high background flaring activity. Photon arrival times in the cleaned event files were corrected to the solar system barycenter using the SAS task `barycen`. We then extracted light curves in the 0.2–10 keV band for all EPIC detectors. For EPIC-pn we extracted a source light curve from a circular region of radius 40'' centered on the source. Background photons were extracted from a circular region of radius 60'' centered on a source-free region on the same chip as the source.

The 0.2–10 keV EPIC-pn light curve is shown in the upper panel of Fig. 1 and shows large amplitude variability. The count rate reaches upwards of 15 counts s^{-1} , meaning we must consider the effects of photon pile-up in the spectra.²⁸ The MOS light curves are not shown here, but the count rate reaches upwards of 4 counts s^{-1} , so we must also consider pile-up when extracting the MOS spectra.

For EPIC-pn, the amplitude of the variability is quite large. To develop a pile-up correction with minimal photon losses, we split our cleaned, barycentered event file into three new event files filtered on source count rate. The first contains times when the source count rate is < 3 counts s^{-1} , the second contains times when the source rate is in the range $3 - 10$ counts s^{-1} , and the third when the source rate is > 10 counts s^{-1} (i.e. the strongest pile-up). We examined the pile-up levels using the SAS task `epatplot`. We then extracted source spectra from each event file, using a circular region of radius 40'' for the < 3 counts s^{-1} event file, an annulus of inner radius 10'' and outer radius 40'' for the $3 - 10$ counts s^{-1} event file, and an annulus of inner radius 12.5'' and outer radius 40'' for the > 10 counts s^{-1} event file. For the highest rate event file, we also only considered single events (PATTERN==0), which are less susceptible to pile-up. Background spectra were extracted from a circular region of radius 60'' centered on a source-free region on the same chip. Response matrices and ancillary responses were generated using the SAS tools `rmfgen` and `arfgen`, respectively. The three count-rate selected

²⁸ The maximum rate for the EPIC-pn to avoid deteriorated response due to photon pile-up in Large Window mode is 3 counts s^{-1} : https://xmmt-tools.cosmos.esa.int/external/xmm_user_support/documentation/uhb/epicmode.html

spectra were combined using `epicspeccombine` to produce a pile-up corrected spectrum. The pn spectrum has been grouped such that each bin has a minimum of 20 counts. A caveat of using `epicspeccombine` is that the tool assumes that the source regions are exactly the same for all co-added spectra. However, this is clearly not the case here, as we utilized different extraction regions depending on the count rate. To remedy this, we include a cross-normalization constant for all spectral fits simultaneous with MOS. As we will see in Section 3.2.2, the spectral shape is consistent across all three EPIC instruments, but the flux is overestimated in the EPIC-pn spectrum and corrected by the cross-normalization constant.

For MOS1 we extracted a source spectrum from an annulus of inner radius $7''.5$ and outer radius $30''$ centered on the source and a background spectrum from a circular region of radius $50''$ centered on a source-free region on the same chip as the source. For MOS2 we extracted a source spectrum from an annulus of inner radius $12''.5$ and outer radius $30''$ centered on the source and a background spectrum from a circular region of radius $40''$ centered on a source-free region on the same chip as the source. Response matrices and ancillary responses were generated using the SAS tools `rmfgen` and `arfgen`, respectively. Spectra from all EPIC instruments have been grouped such that each bin has a minimum of 20 counts.

2.2. Ground-based optical observations

We organized a dedicated ground-based optical observing campaign simultaneous with the *XMM-Newton* observations, which we describe here chronologically. Starting on 2025 March 23 at 18:25 UTC, we observed BG CMi unfiltered and in the g' -band with the 1 m Telescope of the South African Astronomical Observatory (SAAO). We observed the source for approximately 4.5 h with exposure times of 5 s. All exposures were GPS triggered. Master bias frames were created and applied. Data reductions were performed using the PYTHON packages `photutils` v2.2.0 (L. Bradley et al. 2025), Astropy (Astropy Collaboration et al. 2013, 2018, 2022) and `astroquery.gaia`. Calibrated magnitudes from aperture photometry were calculated using 2 field sources present in the European Space Agency *Gaia* Archive²⁹.

On 2025 March 23 at 19:13 UTC, we observed BG CMi using the the Csere Telescope 600/2500 mm at M.R. Štefánik Observatory in Hlohovec, Slovakia using the Atik 383L CCD Camera and the R_c filter. The expo-

sure time was 60 s, and the source was observed for approximately 2 h 43 min. The data were reduced in a standard way using the DAOPHOT package in `IRAF`³⁰, custom-written scripts, and FORTRAN programs created by T. Pribulla (priv. comm.). Initially, master darks and flats were produced. Then all object frames were cleaned from bad pixels and photometrically calibrated. All frames were astrometrically solved to define the pixel to world coordinate system (WCS) transformation, and finally, aperture photometry was performed.

On 2025 March 23 at 20:36 UTC, time-resolved optical photometry of BG CMi was carried out using the CAMELOT-2 instrument on the 82 cm IAC80 telescope in Teide, Tenerife. We used the Johnson B filter with an exposure time of 120 s and obtained a total of 188 images. First, the CAMELOT-2 pipeline software was used to de-bias and flat-field the data. Then the HiPER-CAM pipeline software³¹ was used to extract the target count rates using aperture photometry with a seeing-dependent circular aperture tracking the centroid of the source. The sky background was computed using the clipped mean of an annular region around the target and relative photometry of BG CMi was carried out with respect to a local standard star (A. A. Henden & R. K. Honeycutt 1995; BG CMi-5, with $B=13.16$).

Almost simultaneously, we observed BG CMi in the r' -band with the 1 m Jacobus Kapteyn Telescope (also known as SARA-ORM) at the Roque de los Muchachos, La Palma, Spain, one of the remote facilities operated by the Southeastern Association for Research in Astronomy (SARA; W. C. Keel et al. 2017). We observed the source for approximately 3 h 51 min with exposure times of 20 s. Master calibrations consisting of bias frames and flat fields were created using the Astropy-affiliated PYTHON package `ccdproc` (M. Craig et al. 2017) and applied to the raw science images. The calibrated science images were then aligned in WCS using the `astrometry.net` module included with the Astropy-affiliated `astroquery` PYTHON package (A. Ginsburg et al. 2019). Aperture photometry was performed using `photutils` v2.2.0 (L. Bradley et al. 2025). Calibrated magnitudes were calculated using 7 field sources present in the Pan-STARRS1 catalog (K. C. Chambers et al. 2016; E. A. Magnier et al. 2020).

Starting at 2025 March 24 at 03:38 UTC, BG CMi was also observed with the 0.7 m robotic Great Basin Observatory (GBO) in Great Basin National Park, Nevada, USA for approximately 4 h 15 min, overlapping with

²⁹ <https://gea.esac.esa.int/archive/>

³⁰ <https://github.com/iraf-community/iraf>

³¹ <https://github.com/HiPERCAM/hipercam>

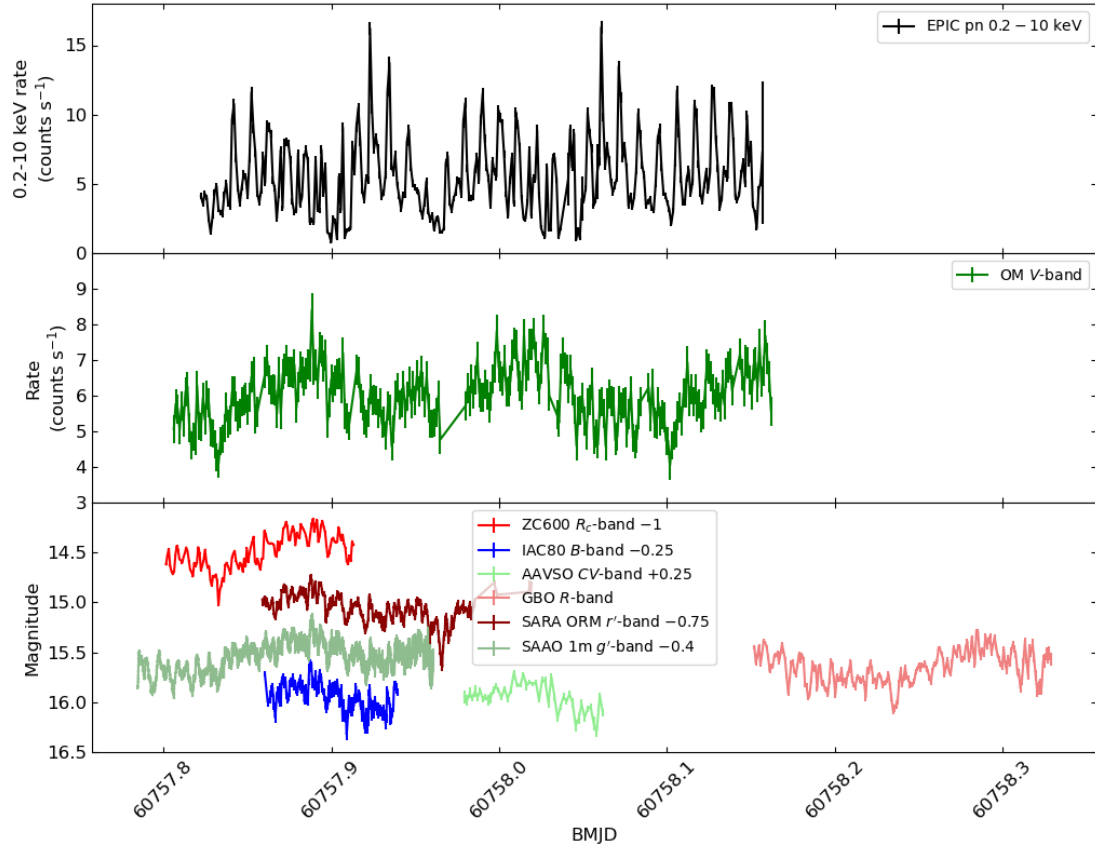


Figure 1. *Upper Panel:* *XMM-Newton*/EPIC-pn 0.2–10 keV light curve of BG CMi with 100 s time resolution. *Middle Panel:* *XMM-Newton*/OM V-band light curve of BG CMi with 100 s time resolution. *:Lower Panel:* Ground-based optical light curves of BG CMi. Filters and telescopes are denoted in the legend. Some light curves have been offset for clarity. All light curves have been corrected to the solar system barycenter and thus times are given in Barycentric Modified Julian Date (BMJD).

the very end of the *XMM-Newton* observation. Observations were performed in the *R*-band, with an exposure time of 60 s per image. Data reduction and plate solving was performed in the same way as for the SARA-ORM images, and aperture photometry was performed using `photutils`. As there were no field stars with calibrated *R*-band magnitudes, we chose 8 field stars with known *r'*- and *i'*-band magnitudes from the Pan-STARRS1 catalog and converted them to *R*-band magnitudes using the K. Jordi et al. (2006) color transformations between photometric systems. We then used the resultant *R*-band magnitudes to calibrate the photometry of BG CMi.

We also utilized public photometry from the American Association of Variable Star Observers (AAVSO) to examine the long-term timing properties of BG CMi. Photometry dating back to June 2020 was downloaded from the AAVSO database and was filtered such that only

CV-band (i.e. unfiltered data with a *V*-band zero-point) was considered as this was the most prevalent data in the archive. We split the data into epochs typically determined by the annual visibility period of BG CMi from the ground. We also filtered the photometry such that no data overlapped in time in the case of two or more observers observing a source simultaneously, prioritizing the observer who provided the most data in each epoch and then including all non-simultaneous data from observers who observed the source during the same epoch. The AAVSO light curves are presented in Fig. 2. We also specifically show the light curve from AAVSO observer J. Hambisch (observer code: HMB) in Fig. 1 as it overlaps with the *XMM-Newton* observation.

All time-series photometry described above has been corrected to the solar system barycenter using Astropy's `time` package.

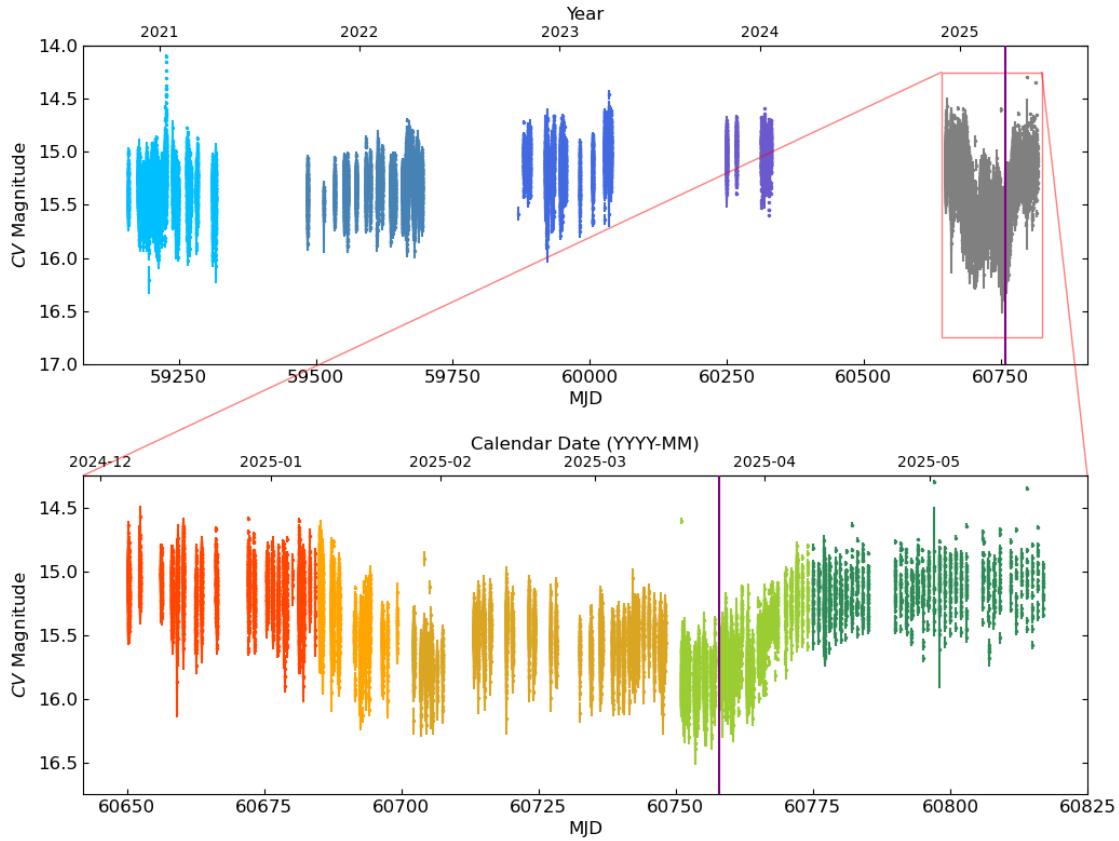


Figure 2. *Upper Panel:* Long-term AAVSO light curve of BG CMi from 2020 to 2025. Observations were taken in a clear filter and calibrated using a V -band zero-point (CV -band). *Lower Panel:* A zoomed in portion of the AAVSO light curve indicated by the red box in the upper panel and highlighting the low state of the source. Colors represent the epochs that we have broken the light curves down into for timing analysis. Though the first four epochs represent individual observing seasons, the low state is split into multiple epochs. In both panels, the purple line represents the time of the *XMM-Newton* observing campaign.

2.3. Additional X-ray observations

2.3.1. Neil Gehrels Swift Observatory

In preparation for the *XMM-Newton* campaign, we also requested Target-of-Opportunity (ToO) observations of BG CMi with the *Neil Gehrels Swift Observatory* (*Swift*) to monitor the flux of the source (A. W. Shaw & C. O. Heinke 2025). Though *Swift* observed BG CMi five times in 2025 March in the lead up to the *XMM-Newton* observation, for the purposes of this work we focus on the longest of those observations. BG CMi was observed by *Swift* on 2025 March 18 at 05:48 UT for 1.9 ks (ObsID: 00088624008). The X-ray Telescope (XRT; D. N. Burrows et al. 2005) operated in photon counting mode. Using XSELECT, spectra were extracted from a circular aperture of radius 20 pixels ($\sim 40''$), centered on the source. Background spectra were extracted from a circular aperture of radius 50 pixels ($\sim 118''$), cen-

tered on a source-free region. An ancillary response file was generated using the FTOOL `xrtmkarf` (included in HEASOFT v6.35.1) and the response matrix file was obtained from the calibration database (CALDB). The 0.3–10 keV *Swift*/XRT count rate was found to be 0.23 counts s^{-1}

We applied the same spectral extraction methodology to two archival *Swift*/XRT observations of BG CMi that occurred when the source was in its typical high state: ObsID 00037144009 (2012 September 06 at 00:20, 7 ks exposure, 0.3–10 keV count rate 0.11 counts s^{-1}) and ObsID 00088624003 (2018 October 12 at 05:30 UT, 4.9 ks exposure, 0.3–10 keV count rate 0.15 counts s^{-1}). For all *Swift*-XRT observations presented in this work, spectra have been grouped such that each bin has a minimum of 20 counts.

2.3.2. *Suzaku*

In order to be able to draw comparisons between the X-ray properties of BG CMi during its low state and those during its ‘normal’ state, we searched the High Energy Astrophysics Science Archive Research Center (HEASARC) for archival X-ray observations of the source. Aside from the *Swift* observations discussed in Section 2.3.1, we also examined a long 2009 *Suzaku* observation. On 2009 April 11 at 12:11 UT, *Suzaku* observed BG CMi for 47 ks (ObsID: 404029010; see T. Yuasa et al. 2010).

In 2009 *Suzaku* (K. Mitsuda et al. 2007) had three operating CCDs that formed the X-ray imaging Spectrometer (XIS), along with the Hard X-ray Detector (HXD). As we are drawing comparisons with *XMM-Newton*, we focus here on the XIS data only. We performed full reprocessing and screening using the FTOOL `Aepipeline` provided by HEASOFT v6.35.1. Source spectra and light curves were extracted from a circular aperture of radius 100'' centered on the source, and background spectra and light curves were extracted from a circular aperture of radius 150'' centered on a source-free region. Response matrices and ancillary responses were generated with the FTOOLS `xisrmfgen` and `xissimarfgen` (Y. Ishisaki et al. 2007), respectively. Spectra from each of the XIS detectors have been grouped such that each bin has a minimum of 20 counts. Light curves were extracted in the 0.2–12 keV energy range for each active detector, and combined with the tool `lcmath`. The combined XIS 0, 1 and 3 light curve had an average 0.2–12 keV count rate of 0.97 counts s⁻¹.

3. ANALYSIS AND RESULTS

3.1. Timing Analysis

For all timing analysis performed in this work, we assume a spin frequency of $\omega = 1.095 \times 10^{-3}$ Hz ($P_{\text{spin}} = 913.5$ s, M. Bonnardeau 2016; J. Patterson et al. 2020) and an orbital frequency of $\Omega = 8.589 \times 10^{-5}$ Hz ($P_{\text{orb}} = 3.23$ h, M. Bonnardeau 2016). We note that the spin period of BG CMi is known very precisely (see also A. Bruch 2025). However, for the purpose of identifying the nature of various peaks in the periodograms, such high precision isn’t required.

3.1.1. *XMM-Newton* Campaign

To investigate the timing properties of BG CMi, we generated Lomb-Scargle periodograms (N. R. Lomb 1976; J. D. Scargle 1982) using the `LombScargle` class included in Astropy. The periodograms of the *XMM-Newton* light curves are shown in Fig. 3, along with a periodogram calculated from the simultaneous ground-based optical light curves. For the ground-based pho-

tometry we only used non-overlapping data, and normalized the light curves in order to reduce the chance of spurious signals appearing in the periodogram. For each periodogram, we calculated a 99.9% significance threshold for the power by randomly shuffling the light curve fluxes (or magnitudes) while keeping the time stamps the same, effectively creating a randomized light curve with the same sampling as the original data. For each panel of Fig. 3 we calculated the peak power for 10,000 such randomized light curves, from which we derived the 99.9% significance threshold.

It is immediately clear from Fig. 3 that the timing properties of BG CMi during the low state are wavelength-dependent. At X-ray energies, the strongest peaks in the periodogram are at the spin frequency ω (and 2ω) and twice the orbital frequency 2Ω . However, there is significant power at numerous sideband frequencies, with the strongest peak at $2\omega - \Omega$. However, at optical wavelengths, the spin, while still significant at the 99.9% level in at least the ground-based light curves, is very weak. Instead, the strongest (non-orbital) timing signature at optical wavelengths is twice the beat frequency, $2(\omega - \Omega)$.

3.1.2. AAVSO

The periodograms in Fig. 3 are just a snapshot of the temporal properties of BG CMi during its low state. In order to investigate the possibility of changing accretion modes, we must compare the timing properties of BG CMi in the low state with those out of it. At optical wavelengths, we can do this by calculating a series of periodograms using the AAVSO light curves presented in Fig. 2. The periodograms are shown in Fig. 4. In panels (a) – (e) we see that the light curves are dominated by variability at Ω and ω . However, as the optical flux of BG CMi starts to decline, so does the strength of the peak at ω , to the point where it is below the 99.9% significance line in panel (g), as noted by C. Littlefield et al. (2025). During the decline and at the base of the low state, we see significant power at $\omega - 2\Omega$ and, in panel (g) only, $\omega - \Omega$. As the flux recovers to levels comparable with those prior to the low state, so does the power at ω .

3.1.3. *Suzaku*

At X-ray energies, we can draw comparisons between the temporal properties of BG CMi during the low state and the ‘normal’ state by performing Lomb-Scargle analysis on the 0.2–12 keV *Suzaku* light curve of BG CMi from 2009. As this is the first reported low state of BG CMi, and there has been continuous optical monitoring of the source annually for many decades (M. Bonnardeau 2016; J. Patterson et al. 2020) with no mention

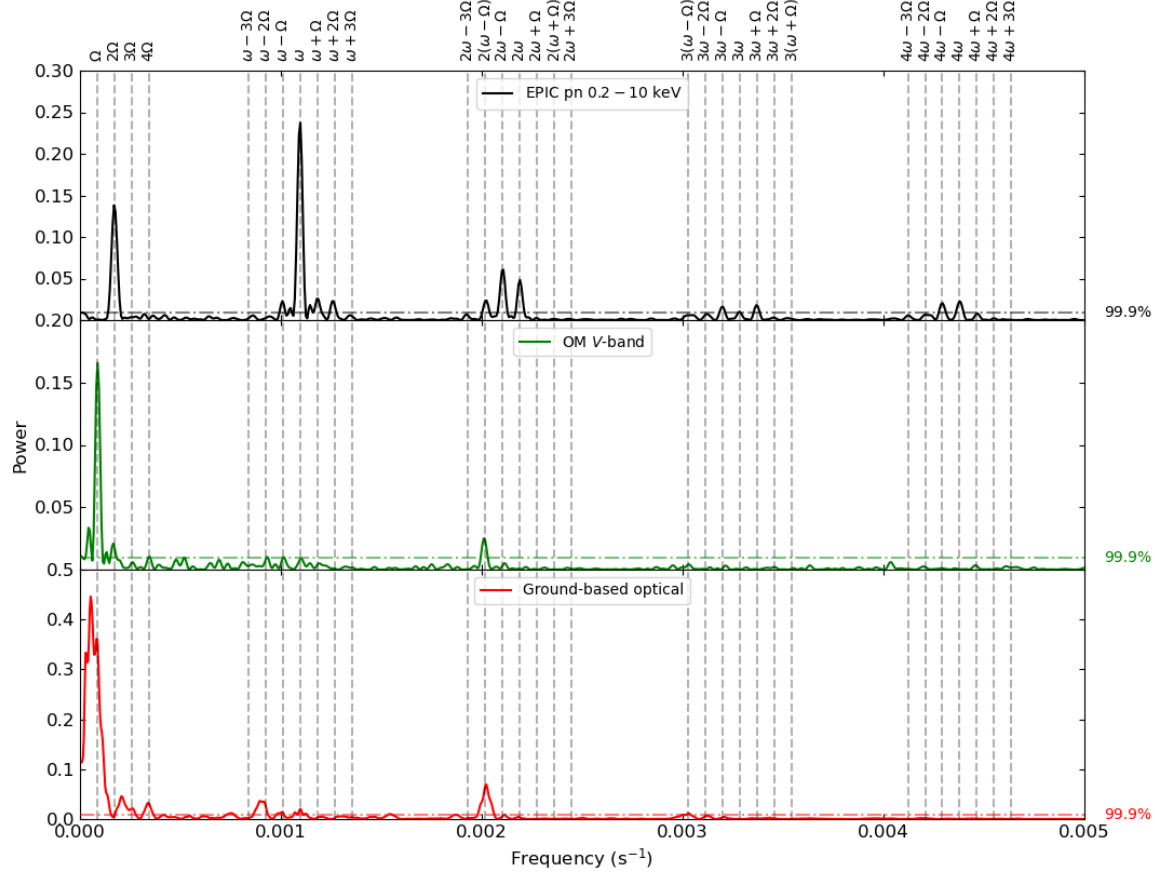


Figure 3. *Upper Panel:* Lomb-Scargle periodogram of the *XMM-Newton* EPIC/pn 0.2–10 keV light curve of BG CMi. *Middle Panel:* Lomb-Scargle periodogram of the *XMM-Newton* EPIC/OM light curve of BG CMi. *Lower Panel:* Lomb-Scargle periodogram of the non-overlapping ground-based optical light curve of BG CMi. In all panels, vertical dashed lines represent known periodicities in the system, including the orbital and spin frequencies (Ω and ω , respectively) and their multiples, as well as beat and sideband frequencies. 99.9% significance thresholds for the Lomb-Scargle power are shown as horizontal dot-dashed lines in each panel.

of a low state in the literature, it is a reasonable assumption that the source was in its typical high state at the time of the *Suzaku* observation.

The *Suzaku* periodogram is shown in Fig. 5. As in Fig. 3, variability at ω (and its harmonics) is highly significant in the X-ray band. In addition, the *Suzaku* periodogram exhibits significant power at Ω and its harmonics, though the strongest peak is at Ω , rather than at 2Ω seen in the *XMM-Newton* periodogram. There are also many $\pm 2\Omega$ spin-orbital sidebands apparently present in the *Suzaku* periodogram. However, we must note that the orbital period of the *Suzaku* satellite ($P_{\text{orb,Suz}} = 96$ min) is coincidentally very close to half the orbital period of BG CMi, such that this may contaminate the Lomb-Scargle analysis. Despite this, a key difference between the *XMM-Newton* EPIC/pn and *Suzaku* periodograms is the presence of significant variability at

$2\omega - \Omega$ and $2(\omega - \Omega)$ during the low state (Fig. 3; upper panel), which is not present in the *Suzaku* periodogram. In addition, the *XMM-Newton* EPIC/pn periodogram also shows statistically significant power at the $\pm \Omega$ spin-orbital sidebands that is not present in the archival *Suzaku* observation.

3.2. X-ray Spectral Analysis

In Fig. 6 we show three 0.5–10 keV *Swift*/XRT snapshots of BG CMi from 2012, 2018 and 2025, with the 2025 observation having occurred during the low state. Even a simplistic comparison such as this highlights a drastic change in the X-ray properties of BG CMi during the low state, with a large increase in soft flux. To investigate this further, we must model the X-ray spectra of BG CMi both in and out of the low state.

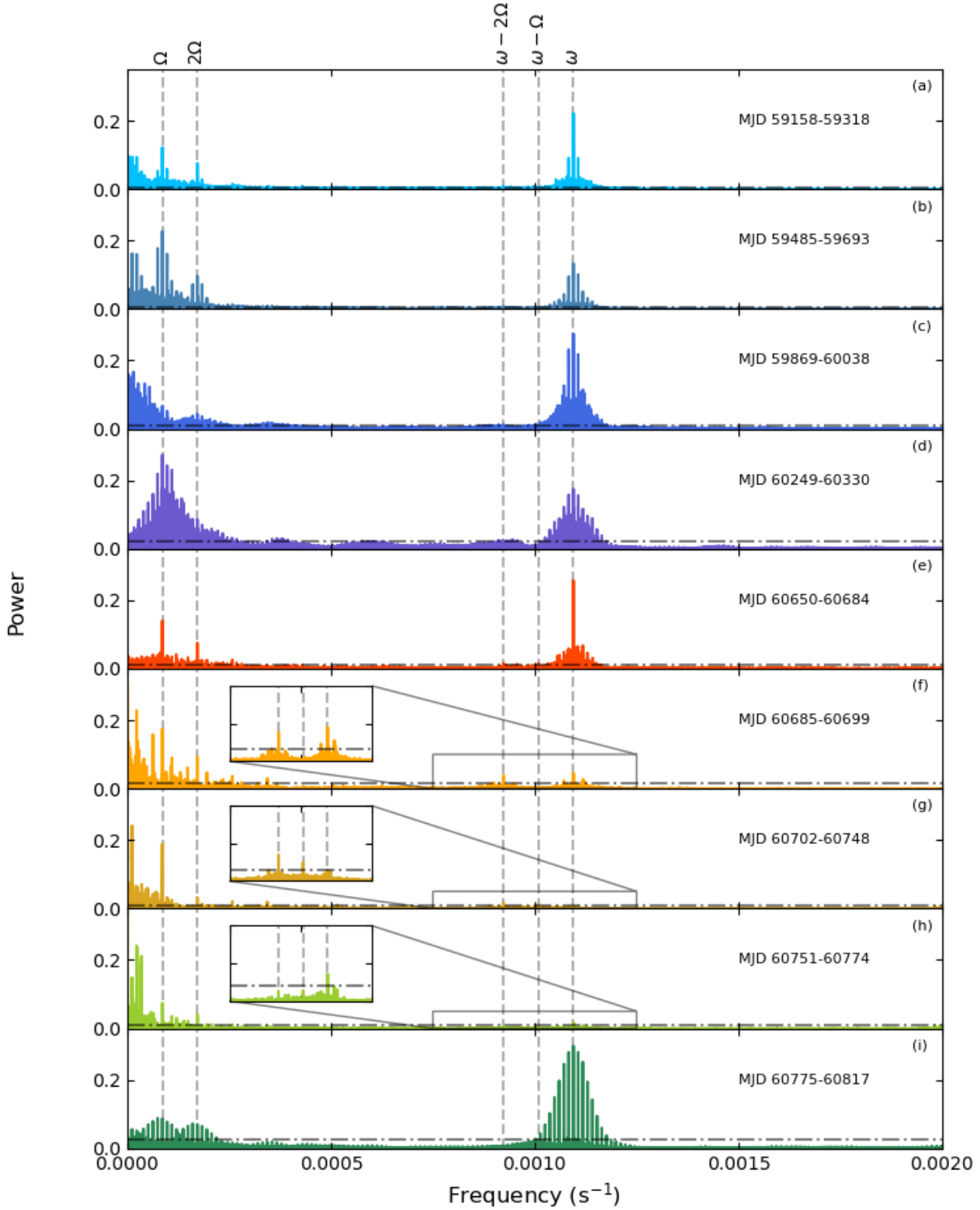


Figure 4. Lomb-Scargle periodograms of the AAVSO light curves of BG CMi. The colors match the epochs defined in Fig. 2, and the relevant MJD ranges are labeled in each panel. The vertical dashed lines represent known periodicities related to the system and the dot-dashed horizontal lines in each panel indicated the 99.9% confidence level.

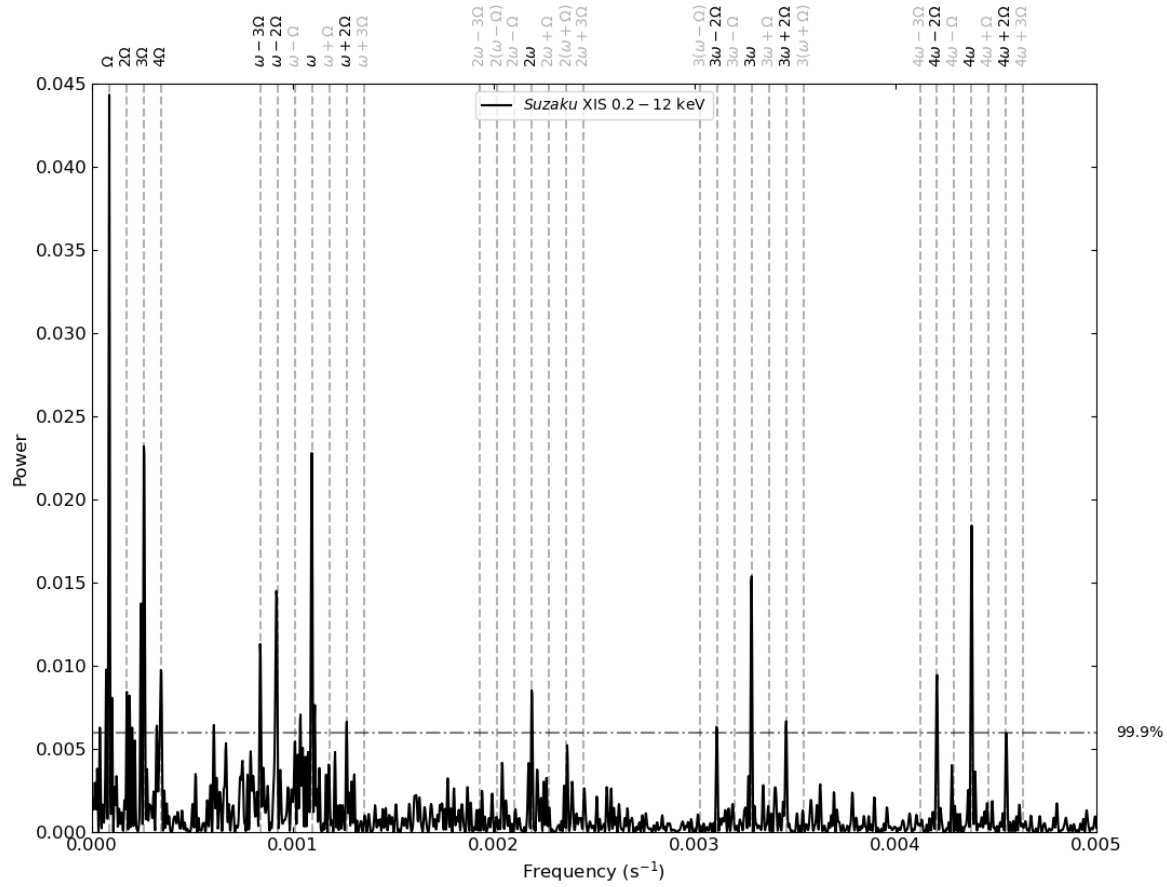


Figure 5. Lomb-Scargle periodogram of the 2009 Apr 11 *Suzaku* 0.2–12 keV light curves of BG CMi. The vertical dashed lines represent known periodicities related to the system, with undetected periods shown in grey at the top of the figure. The dot-dashed horizontal line represents the 99.9% confidence level.

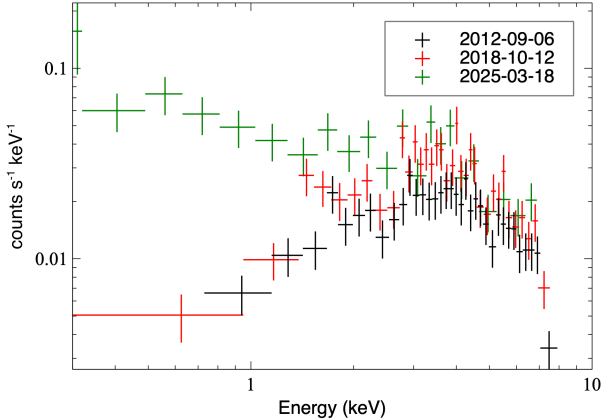


Figure 6. *Swift/XRT* spectra of BG CMi taken during its regular high state (2012 and 2018; black and red, respectively) and the low state (2025; green). No models have been fit to the spectra.

Here, we model the X-ray spectra from the typical high state of BG CMi (*Suzaku*) and from the low state (*XMM-Newton*). All modeling is performed in XSPEC v12.15.0 using J. Wilms et al. (2000) abundances, D. A. Verner et al. (1996) photoionization cross-sections and the χ^2 fitting statistic.

3.2.1. The *Suzaku* high state spectrum

H. Ezuka & M. Ishida (1999) present a 0.5–10 keV Advanced Satellite for Cosmology and Astrophysics Solid-state Imaging Spectrometer and Gas Imaging Spectrometer (*ASCA/SIS* and *GIS* Y. Tanaka et al. 1994) spectrum of BG CMi as part of a survey of 23 mCVs. H. Ezuka & M. Ishida (1999) found that the 0.5–10 keV spectrum could be well-described by a thermal bremsstrahlung model modified by three partial covering absorbers, in addition to three Gaussians to represent the iron line complex in the 6–7 keV range. This is a common way to model the X-ray spectra of IPs, though sometimes one or two single-temperature thermal plasmas are used in place of the thermal bremsstrahlung component (see e.g. K. Mukai et al. 2015; M. R. Kennedy et al. 2017).

We fit the model of H. Ezuka & M. Ishida (1999) to the archival *Suzaku*/XIS spectra of BG CMi in the 0.8–10 keV energy range. We ignore photons with energies 1.7–1.9 keV and 2.2–2.4 keV due to calibration issues in those energy ranges. The full model, as written in XSPEC notation is `constant*pcfabs*pcfabs*pcfabs*(bremss+gaussian)`, where `constant` represents a cross-normalization constant between the three XIS detectors. We note that H. Ezuka & M. Ishida (1999) do not include an interstellar absorption component such as `tbabs` (J. Wilms et al.

2000). We find an acceptable fit, with $\chi^2_\nu = 1.13^{32}$ ($\chi^2/\text{dof} = 1897/1682$). However, we find that one of the partial covering components is poorly constrained, with an unbound N_{H} and covering fraction. Thus we consider it an unnecessary inclusion in the model.

We then model the *Suzaku* spectrum of BG CMi with an isobaric cooling flow model (R. F. Mushotzky & A. E. Szymkowiak 1988; K. Mukai et al. 2003), modified by two partial covering components and an interstellar absorption component, which we freeze to the Galactic value of $N_{\text{H}} = 0.06 \times 10^{22} \text{ cm}^{-2}$ (HI4PI Collaboration et al. 2016). The cooling flow model (`mkcfflow` in XSPEC) has been used to successfully describe the X-ray spectra of many IPs (see e.g. K. Mukai et al. 2015) and is a much more accurate physical representation of the post-shock flow above the surface of the WD than a single-temperature bremsstrahlung model. (Even more detailed post-shock models have been constructed to fit the full spectra of IPs, extending up to ~ 80 keV, e.g. V. Suleimanov et al. 2005; T. Yuasa et al. 2010; V. F. Suleimanov et al. 2019. As we do not use data above 10 keV or attempt to constrain the WD mass, the current model is sufficient.) In `xspect` notation, our model is written as `constant*tbabs*pcfabs*pcfabs*(mkcfflow + gaussian)`, where the additional Gaussian component represents the neutral Fe K α line. We find that this model describes the high-state spectrum well ($\chi^2_\nu = 1.12$; 1683 dof) and we list the best-fit parameters in Table 1. We choose two partial covering components to represent two distinct components of the intrinsic absorber. BG CMi shows grazing eclipses in the optical (see Fig. 1), and thus is a moderately inclined binary ($i \sim 55^\circ - 75^\circ$; D. de Martino et al. 1995). Therefore, we might expect some of the intrinsic absorption to come from the disk, similar to FO Aqr (P. A. Evans et al. 2004; M. R. Kennedy et al. 2017), while some will come from the pre-shock flow, as for the majority of IPs (see e.g. K. Mukai 2017). We call the model with two partial covering components ‘Model 1’.

C. Done & P. Magdziarz (1998) note that multiple discrete partial covering models, each with their own hydrogen column densities (N_{H}) and covering fractions (f), are a poor approximation for the complex absorption of X-ray photons by the pre-shock flow. A distribution of covering fractions as a function of N_{H} , approximated as a power law, provides a much more physical representation of the absorption. We therefore replace one of the partial covering components with an ionized complex absorber `zxicpab` (N. Islam & K. Mukai

³² Reduced chi-squared statistic: χ^2 per degrees of freedom (dof)

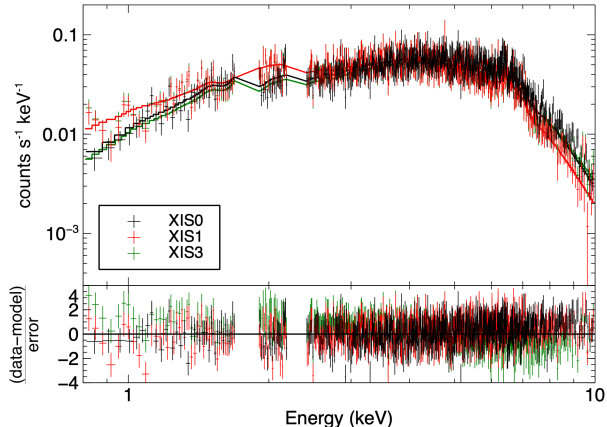


Figure 7. Archival *Suzaku*/XIS spectra of BG CMi during the high state. The spectra have been fit with a cooling flow model modified by partial covering and a complex absorber, denoted Model 2 in the text. Residuals are shown in the lower panel.

2021), a modification to the C. Done & P. Magdziarz (1998) model. We call this model ‘Model 2’ and it is written as `constant*tbabs*pcfabs*zxipab*(mkcfflow + gaussian)` in `xspec` notation. We find that Model 2 results in a marginally better fit than Model 1 ($\Delta\chi^2 = -6$; for one fewer dof). However, they are almost indistinguishable. We therefore show the best fit parameters for both models in Table 1.

We find hydrogen column densities of $N_{\text{H,pc1}} = 3.2 \pm 0.4 \times 10^{22} \text{ cm}^{-2}$ and $N_{\text{H,pc2}} = 14.2_{-1.9}^{+3.1} \times 10^{22} \text{ cm}^{-2}$ with covering fractions of $f_{\text{pc1}} = 0.93 \pm 0.01$ and $f_{\text{pc2}} = 0.67 \pm 0.04$ for the first and second partial covering components in Model 1, respectively, indicating significant intrinsic absorption. In Model 2, we find $N_{\text{H,pc1}} = 3.2_{-0.5}^{+1.2} \times 10^{22} \text{ cm}^{-2}$ and $f_{\text{pc1}} = 0.78_{-0.15}^{+0.06}$ for the lone partial covering component. For the complex absorber in Model 2, we find a maximum column density $N_{\text{H,max}} = 20.2_{-4.6}^{+9.3} \times 10^{22} \text{ cm}^{-2}$ with a power-law index of the covering fraction $\beta = -0.38_{-0.12}^{+0.18}$ (where $f \propto N_{\text{H}}^\beta$ and $\int_{N_{\text{H,min}}}^{N_{\text{H,max}}} f = 1.0$; N. Islam & K. Mukai 2021).³³ A negative value of β is indicative of a decreasing value of f with increasing N_{H} and, in the specific case of the fit to the *Suzaku* spectrum of BG CMi in the high state, $f = 0$ at $N_{\text{H}} = 20.2_{-4.6}^{+9.3} \times 10^{22} \text{ cm}^{-2}$.

We find an absorbed flux of $\approx 1.8 \times 10^{-11} \text{ erg cm}^{-2} \text{ s}^{-1}$ in the 0.5–10 keV energy range, with almost all of that flux emerging in the 2–10 keV band ($\approx 1.8 \times 10^{-11}$). We find an unabsorbed flux of $\approx 3.7 \times 10^{-11} \text{ erg cm}^{-2}$

³³ We freeze the minimum column density to $N_{\text{H,min}} = 10^{15} \text{ cm}^{-2}$, essentially zero.

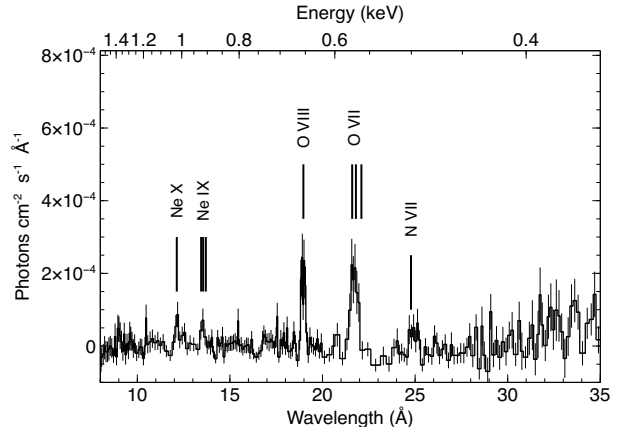


Figure 8. Residuals of a phenomenological fit to the *XMM-Newton*/RGS spectrum of BG CMi, with some spectral features labeled.

s^{-1} and $\approx 2.7 \times 10^{-11} \text{ erg cm}^{-2} \text{ s}^{-1}$ in the 0.5–10 keV and 2–10 keV bands, respectively. The quoted fluxes are for Model 1, but we find consistent results for Model 2. We plot the *Suzaku* spectra and the Model 2 fit in Fig. 7.

3.2.2. The *XMM-Newton* low state spectrum

We model the 0.5–10 keV low-state *XMM-Newton*/EPIC spectra of BG CMi in a similar manner to the *Suzaku* spectra, using Model 1 and Model 2. However, the initial fit reveals a low-energy excess below $\lesssim 0.8$ keV. To investigate this excess further we reduce and combine the data from the two Reflection Grating Spectrometer (J. W. den Herder et al. 2001, RGS;) detectors onboard *XMM-Newton*. We used the `rgsproc` and `rgscombine` tasks in SAS and fit a phenomenological model of an absorbed power law (with partial covering; `tbabs*pcfabs*powerlaw`) to the resultant spectrum and plot the residuals in Fig. 8. Though we do not make any attempt to statistically identify lines (for example through a blind search, e.g. A. W. Shaw et al. 2022), it is clear that there are narrow lines present, with the strongest being coincident with the rest wavelengths of O VIII Ly α and the O VII He-like triplet.

We therefore include an additional Gaussian component in our models when fitting the *XMM-Newton*/EPIC spectra of BG CMi, initialized at a line energy of 0.6 keV, to account for the unresolved oxygen lines. The updated Model 1 is thus `constant*tbabs*pcfabs*pcfabs*(mkcfflow + gaussian + gaussian)`, while Model 2 becomes `constant*tbabs*pcfabs*pcfabs*zxipab*(mkcfflow + gaussian + gaussian)`. We find that both models describe the data very well, with fit statistics of $\chi^2_\nu = 1.02$

Table 1. Best-fit parameters of two model fits to the X-ray spectra of BG CMi from two epochs. The *Suzaku* observations occurred when the source was in its typical high state, while the *XMM-Newton* observations took place during the 2025 low state. Models are described in the text, but we incorporate an additional Gaussian (G2) when modeling the *XMM-Newton* spectra to represent unresolved emission lines below 1 keV.

Parameter	<i>Suzaku</i> (high state)		<i>XMM-Newton</i> (low state)	
	Model 1	Model 2	Model 1	Model 2
N_{H} ($\times 10^{22} \text{ cm}^{-2}$)	0.06*	0.06*	0.06*	0.06*
$N_{\text{H,pc1}}$ ($\times 10^{22} \text{ cm}^{-2}$)	3.2 ± 0.4	$3.2_{-0.5}^{+1.2}$	2.9 ± 0.4	$7.3_{-1.4}^{+2.1}$
f_{pc1}	0.93 ± 0.01	$0.78_{-0.15}^{+0.06}$	$0.63_{-0.04}^{+0.02}$	$0.30_{-0.09}^{+0.07}$
$N_{\text{H,pc2}}$ ($\times 10^{22} \text{ cm}^{-2}$)	$14.2_{-1.9}^{+3.1}$...	$28.5_{-5.1}^{+5.8}$...
f_{pc2}	0.67 ± 0.04	...	0.55 ± 0.04	...
$N_{\text{H,max}}$ ($\times 10^{22} \text{ cm}^{-2}$)	...	$20.2_{-4.6}^{+9.3}$...	> 64.7
β	...	$-0.38_{-0.12}^{+0.18}$...	-0.68 ± 0.04
$\log_{10} \xi$...	$0.3_{-0.7}^{+0.6}$...	0.6 ± 0.2
T_{max} (keV)	> 42.7	$20.2_{-4.6}^{+9.3}$	$34.1_{-6.6}^{+17.5}$	$24.3_{-3.3}^{+9.9}$
abundance (rel. to solar)	$0.49_{-0.16}^{+0.17}$	$0.28_{-0.10}^{+0.22}$	$0.35_{-0.11}^{+0.15}$	$0.25_{-0.06}^{+0.07}$
Normalization (<code>mkcfflow</code> ; $\times 10^{-10} M_{\odot} \text{ yr}^{-1}$)	$4.7_{-0.8}^{+2.4}$	$7.6_{-4.2}^{+3.7}$	$9.5_{-3.1}^{+2.4}$	$16.5_{-6.1}^{+22.5}$
E_{G1} (keV)	$6.40_{-0.03}^{+0.04}$	6.40 ± 0.03	$6.40_{-0.03}^{+0.04}$	6.40 ± 0.03
σ_{G1} (keV)	$0.12_{-0.05}^{+0.06}$	0.09 ± 0.05	0.09 ± 0.06	< 0.11
Normalization (G1; $\times 10^{-5} \text{ photon cm}^{-2} \text{ s}^{-1}$)	$3.7_{-0.8}^{+0.9}$	$3.0_{-0.7}^{+0.8}$	$4.0_{-1.0}^{+1.2}$	$4.0_{-1.1}^{+4.4}$
E_{G2} (keV)	$0.54_{-0.02}^{+0.01}$	$0.52_{-0.05}^{+0.03}$
σ_{G2} (keV)	0.08 ± 0.01	$0.10_{-0.02}^{+0.03}$
Normalization (G2; $\times 10^{-3} \text{ photon cm}^{-2} \text{ s}^{-1}$)	$4.5_{-0.9}^{+1.0}$	$8.8_{-2.8}^{+15.3}$
C_{XIS1}	1.09 ± 0.02	1.09 ± 0.02
C_{XIS3}	0.82 ± 0.02	0.82 ± 0.02
C_{pn}	0.67 ± 0.01	0.67 ± 0.01
C_{MOS1}	0.98 ± 0.02	0.98 ± 0.02
$F_{\text{abs},0.5-10}$ ($\times 10^{-11} \text{ erg cm}^{-2} \text{ s}^{-1}$)	1.8 ± 0.3	1.8^{\dagger}	$2.3_{-1.2}^{+1.1}$	2.3^{\dagger}
$F_{\text{unabs},0.5-10}$ ($\times 10^{-11} \text{ erg cm}^{-2} \text{ s}^{-1}$)	3.7 ± 0.1	3.9 ± 0.3	5.0 ± 0.3	$6.9_{-1.1}^{+6.0}$
$F_{\text{abs},2-10}$ ($\times 10^{-11} \text{ erg cm}^{-2} \text{ s}^{-1}$)	1.8 ± 0.2	1.8^{\dagger}	$2.0_{-1.0}^{+1.3}$	2.0^{\dagger}
$F_{\text{unabs},2-10}$ ($\times 10^{-11} \text{ erg cm}^{-2} \text{ s}^{-1}$)	2.7 ± 0.1	2.6 ± 0.2	$3.2_{-0.1}^{+0.2}$	$4.0_{-0.6}^{+3.7}$
χ^2/dof	1886/1683	1880/1682	1940/1894	1929/1893

* Frozen

† Error analysis did not converge

N_{H} : Hydrogen column density

$N_{\text{H,pc1/2}}$: Hydrogen column density for partial covering component 1/2

$f_{\text{pc1/2}}$: Covering fraction for partial covering component 1/2

$N_{\text{H,max}}$: Maximum hydrogen column density for the `zxipab` model component

β : Covering fraction power-law index ($f = N_{\text{H}}^{\beta}$)

$\log_{10} \xi$: Ionization parameter

T_{max} : Maximum temperature of the cooling flow

$E_{\text{G1/2}}$: Central energy of Gaussian 1/2

$\sigma_{\text{G1/2}}$: Width of Gaussian 1/2

C : Cross-normalization constant (relative to XIS2 for *Suzaku* and MOS1 for *XMM-Newton*)

$F_{\text{abs/unabs}}$: Absorbed/unabsorbed flux in the indicated energy band

(1894 dof) and $\chi^2_\nu = 1.02$ (1893 dof) for Model 1 and 2, respectively. Similar to the *Suzaku* model fits, Model 2 results in a marginally better fit than Model 1 ($\Delta\chi^2 = -11$; for one fewer dof) but we must note that $N_{\text{H},\text{max}}$ is unconstrained in the best-fit Model 2. We also remind the reader that the cross-normalization constant to EPIC-pn, C_{pn} , is significantly lower than unity, owing to our piecewise pile-up correction method detailed in Section 1. The spectral shape in EPIC-pn is consistent with that measured by the MOS detectors.

For Model 1, we find $N_{\text{H},\text{pc1}} = 2.9 \pm 0.4 \times 10^{22} \text{ cm}^{-2}$ and $N_{\text{H},\text{pc2}} = 28.5^{+5.8}_{-5.1} \times 10^{22} \text{ cm}^{-2}$ with covering fractions of $f_{\text{pc1}} = 0.63^{+0.02}_{-0.04}$ and $f_{\text{pc2}} = 0.55 \pm 0.04$, respectively. The covering fractions are significantly smaller than the best-fit values for the *Suzaku* spectrum, indicating a drastic reduction in absorption local to the source. For Model 2, we find $N_{\text{H},\text{pc1}} = 7.3^{+2.1}_{-1.4} \times 10^{22} \text{ cm}^{-2}$ and $f_{\text{pc1}} = 0.30^{+0.07}_{-0.09}$ for the lone partial covering component, once again indicating a drastic reduction in local absorption. For the complex absorber, we find a maximum column density $N_{\text{H},\text{max}} > 64.7 \times 10^{22} \text{ cm}^{-2}$ and $\beta = -0.68 \pm 0.04$, which is significantly steeper (and for a higher $N_{\text{H},\text{max}}$) than in the high state.

We find an absorbed flux of $2.3 \times 10^{-11} \text{ erg cm}^{-2} \text{ s}^{-1}$ in the 0.5–10 keV energy range and 2.0×10^{-11} in the 2–10 keV band. We find an unabsorbed flux of $5.0 \times 10^{-11} \text{ erg cm}^{-2} \text{ s}^{-1}$ and $3.2 \times 10^{-11} \text{ erg cm}^{-2} \text{ s}^{-1}$ in the 0.5–10 keV and 2–10 keV bands, respectively. The quoted fluxes are for Model 1, but we find the unabsorbed fluxes in Model 2 have large uncertainties due to the unconstrained value of $N_{\text{H},\text{max}}$. Regardless, we find that the X-ray flux of BG CMi has not decreased alongside the optical flux during the low state when compared with the archival *Suzaku* data and, in fact, appears to have increased overall. As Fig. 6 suggests, there is a significant increase in soft X-ray flux during the low state, coincident with the decrease in intrinsic absorption. We show the *XMM-Newton* spectra, fit with Model 2, in Fig. 9.

4. DISCUSSION

Although low states have been studied in numerous IPs (e.g. P. Garnavich & P. Szkody 1988; M. R. Kennedy et al. 2017; C. Littlefield et al. 2020; A. E. Covington et al. 2022), this marks only the second time that deep X-ray observations of an IP low state have been reported (after FO Aqr; M. R. Kennedy et al. 2017). X-rays allow us to study the post-shock region close to the surface of the white dwarf, whereas optical photons mostly originate in the accretion disk. Simultaneous optical and X-ray observations allow us to develop a more complete picture of the accretion flow during a low state. More-

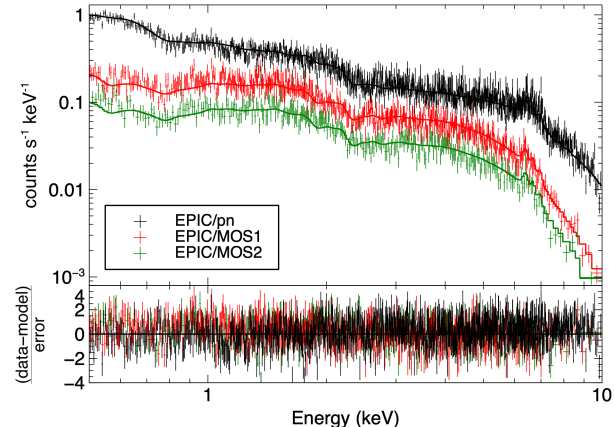


Figure 9. *XMM-Newton*/EPIC spectra of BG CMi during the low state in March 2025. The spectra have been fit with Model 2. Residuals are shown in the lower panel.

over, BG CMi is well-studied enough that we can make meaningful comparisons with observations made during its typical high state.

4.1. Optical and X-ray timing

Fig. 2 highlights the dense optical photometric coverage of BG CMi by observers of the AAVSO, and we show the evolution of the timing properties in the optical band in Fig. 4. The X-ray coverage, by comparison, is much more sparse. However, we are able to draw comparisons between the X-ray timing properties in the high state and the low state by examining an archival *Suzaku* observation of BG CMi.

In Fig. 4 we see that the optical light curves of BG CMi are typically dominated on short (sub-h) timescales by variability at the spin frequency of the WD, ω . However, as the optical flux starts to decline, so does the strength of the variability. In panel (g), when the optical light curve (Fig. 2) appears to have bottomed out, the spin variability is no longer significant at the 99.9% level and instead the strongest short term variability, though still weak, is at $\omega - 2\Omega$. This change in the dominant frequencies in the optical periodogram is indicative of a change in the accretion mode of the IP. A typical, disk-fed IP will show strong variability on the spin period of the WD due to matter being forced onto field lines at a nearly uniform rate from a Keplerian disk whose inner radius co-rotates with the WD. If, instead, the matter flows from a fixed point in the binary rest frame (stream-fed accretion), the optical variability will appear at an orbital sideband. This change away from a strong signal at ω is often associated with low states (e.g. C. Littlefield et al. 2020; A. E. Covington et al. 2022).

In Fig. 3 we show the multi-wavelength timing properties of BG CMi during the low state. In the lower two panels we confirm the near-disappearance of the spin variability at optical wavelengths that was seen in the AAVSO periodograms. We also see the emergence of variability on timescales consistent with the $\omega - 2\Omega$ and $2(\omega - \Omega)$ frequencies. In the upper panel we see that, while the spin of the WD dominates the X-ray light curves, there is significant power at $\omega - \Omega$ and $2\omega - \Omega$ that is not present in the archival *Suzaku* light curves from the high state (Fig. 5). Much like with the AAVSO periodograms (Fig. 4), this is strongly indicative of a change in accretion mode.

Interestingly, the top panel of Fig. 3 shows a strong peak at 2Ω , while the optical periodograms in the middle and lower panels show variability at Ω , consistent with the orbital variability of the binary. When comparing the *XMM-Newton* EPIC-pn periodogram with that derived from archival *Suzaku* light curves in Fig. 5 it is clear that the dominant orbital variability has switched from Ω to 2Ω at X-ray energies.³⁴ This is another indication that the accretion mode has changed.

According to the L. Ferrario & D. T. Wickramasinghe (1999) model, a switch to a stream-only accretion mode of a moderate-highly inclined source like BG CMi should result in the emergence of strong power at sidebands such as $2\omega - \Omega$ at X-ray energies.³⁵ Simultaneously, the model predicts that, at optical wavelengths, strong power emerges at $\omega - 2\Omega$ and $2(\omega - \Omega)$. The emergence of power at these frequencies in the low-state periodograms in Figs. 3 and 4f,g suggests that the accretion stream had become more important during the low state. The near complete disappearance of ω in the optical periodograms during the low state (Figs. 3 and 4g) may even suggest that the disk had almost completely dissipated, but this cannot be confirmed with optical timing analysis alone. The significant reduction in optical flux, which is dominated by the disk and hotspot in IPs, supports the hypothesis that the disk mass significantly decreased during the low state. We note here that L. Ferrario & D. T. Wickramasinghe (1999) modeled the power spectrum of intrinsic optical emission from IPs and acknowledged that a full model would also need to consider reprocessing of X-rays, though the model is still a useful reference when discussing accretion modes in IPs.

³⁴ We also note that Ω dominates in the 0.7–10 keV *ASCA* light curves (T. L. Parker et al. 2005)

³⁵ We note that L. Ferrario & D. T. Wickramasinghe (1999) mislabel this as $\omega - 2\Omega$ in their Fig. 5.

However, the L. Ferrario & D. T. Wickramasinghe (1999) model does not account for the increased variability at 2Ω at X-ray energies that we see during the low state of BG CMi. To resolve this, we consider the possibility that disk-overflow accretion might be a valid mechanism to explain this observed phenomenon. C. Hellier (1993) shows that the X-ray light curves of FO Aqr are compatible with a hybrid model of accretion in which accreting material flows both through a disk and a stream above the disk, known as disk-overflow. C. Hellier (1993) showed that the orbital modulation in the disk-overflow IP FO Aqr manifests in the form of two energy-dependent dips per orbit in the X-ray light curves. The energy dependence of the dips implies photoelectric absorption caused by increased scale height obscuring the X-ray emission at two locations: where the stream from the secondary hits the outer edge of the disk, and where the overflow stream hits the magnetosphere. To test if this mechanism is responsible for the 2Ω peak in the X-ray power spectrum of BG CMi during the low state, we generated Lomb-Scargle periodograms of the soft (0.2–2 keV) and hard (2–10 keV) *XMM-Newton* light curves and plot them in Fig. 10. We find that the vast majority of the power at 2Ω is found in the soft band and that the orbital variability in the hard band is almost all at Ω . This is consistent with the C. Hellier (1993) disk-overflow accretion model and thus implies that BG CMi is undergoing disk-overflow accretion during the low state, at least during the time of the *XMM-Newton* observations.

We also consider the possibility of a double-armed spiral wave structure in the disk (generated by tides), which might generate two splash points where the arms meet the magnetosphere (J. R. Murray et al. 1999), and thus variability in X-ray absorption at 2Ω . However, an argument against this scenario is that increased spiral-wave structure is thought to be more, not less, efficient at angular momentum transport, making the disk brighter, not fainter (J. R. Murray et al. 1999). We thus prefer the disk-overflow accretion model.

4.2. X-ray spectroscopy

In Fig. 6 we show the drastic difference in the *Swift*/XRT X-ray spectrum of BG CMi between the normal high state and the low state. Contrary to what we see in the optical, during the low state, the observed (absorbed) X-ray flux of BG CMi did not decrease relative to the high state. In fact, when examining the unabsorbed fluxes, we find a slight increase.

When modeling the X-ray spectra, the most striking difference we found was a significant reduction in absorption local to the system. When considering the model

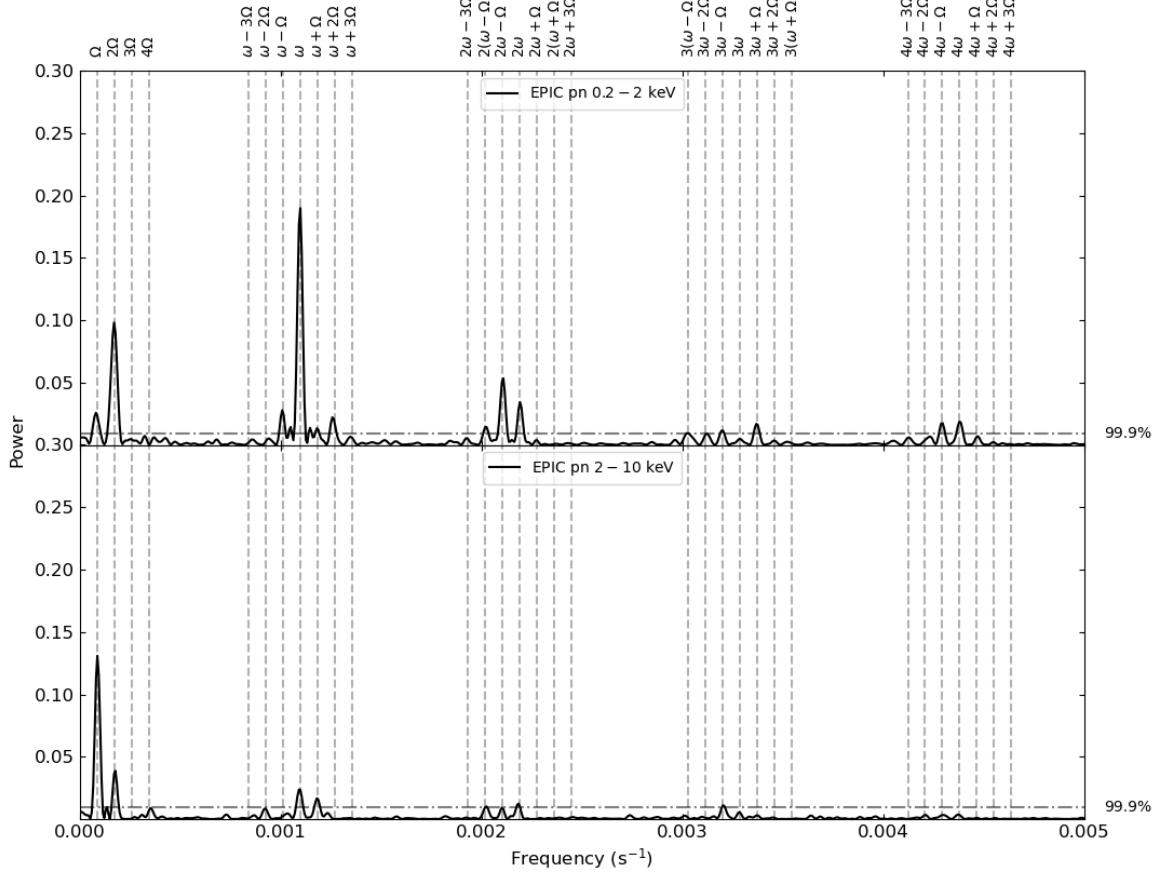


Figure 10. *Upper Panel:* Lomb-Scargle periodogram of the *XMM-Newton* EPIC/pn 0.2–2 keV light curve of BG CMi. *Lower Panel:* Lomb-Scargle periodogram of the EPIC/pn 2–10 keV light curve of BG CMi. As in Fig. 3, vertical dashed lines represent known periodicities in the system.

with two simple partial covering components (Model 1), we find that the covering fraction of the first `pcfabs` component decreases from 93% to 63%, while the covering fraction of the second `pcfabs` component decrease less drastically, from 67% to 55%. When utilizing a partial covering absorber combined with a complex absorber to represent absorption from the pre-shock flow (`zxipab`; Model 2) we find that the covering fraction from the `pcfabs` component, representing the absorption of X-ray photons by the disk, significantly decreases from 78% to 30%.

This significant decrease in covering fraction in both Model 1 and Model 2 is consistent with the hypothesis we presented in Section 4.1, i.e. that the disk had, at least partially, dissipated during the low state. Decreasing the mass of the disk in a moderately inclined source like BG CMi decreases the likelihood of a photon being absorbed by the disk in the observer’s line of sight.

The fact that the X-ray flux did not decrease between the typical high state low state implies that the mass-accretion rate on to the WD (\dot{M}_{WD}) also did not decrease. This is contrary to what was seen during the 2016 low state of FO Aqr, which showed a dramatic decrease in X-ray flux relative to an archival high state observation, indicative of a reduction in \dot{M}_{WD} (M. R. Kennedy et al. 2017). The earliest X-ray observation of BG CMi during the 2025 low state took place on 2025-03-05 (MJD 60739), measuring $F_{\text{unabs}, 0.5-10} = 4.6^{+3.7}_{-1.1} \times 10^{-11} \text{ erg cm}^{-2} \text{ s}^{-1}$ with *Swift*/XRT (A. W. Shaw & C. O. Heinke 2025). This implies that \dot{M}_{WD} was comparable with the high state value from at least this date. However, there is no direct indication of \dot{M}_{WD} from the earliest part of the low state. We therefore cannot be certain that \dot{M}_{WD} ever decreased.

4.3. Timeline of the low state of BG CMi

Combining the multi-epoch, multi-wavelength timing data with the X-ray spectroscopy from both the high

and low states of BG CMi allows us to build up a near-complete picture of the physics of the low state. During the high state, BG CMi can be considered to be a typical IP, in which the WD accretes matter via a partial accretion disk (the disk-fed accretion mode). However, in January 2025, the optical flux of BG CMi decreased, indicative of the disk dissipating significantly. Though we are unable to determine whether or not \dot{M}_{WD} decreased at any point during the low state, the dissipation of the disk implies that the mass-transfer rate from the companion on to the disk $\dot{M}_2 < \dot{M}_{\text{WD}}$, at least during the initial decline in optical flux (MJD $\sim 60685 - 60699$; the orange portion of the light curve in Fig. 2). The dissipation of the accretion disk is not only supported by the drop in optical flux, but also by the optical periodograms in Fig. 4, which show a significant decrease in optical power at the spin frequency.

A. E. Covington et al. (2022) note that at least one IP, DO Dra shows evidence of a complete cessation of accretion during a low state, with the white dwarf and its companion being the sole contributor to the optical flux. Therefore, we considered the possibility that the hot white dwarf contributed to the optical flux in the low state. C. Knigge et al. (2011) show that the WD in BG CMi ($P_{\text{orb}} = 3.23$ h) should have an effective temperature $T_{\text{eff}} \sim 25000$ K. The median absolute V -band magnitude for a WD in the range 20000 – 30000 K is $M_V \sim 10$ (P.-E. Tremblay et al. 2011). The measured distance to BG CMi of $d = 867^{+26}_{-24}$ pc (C. A. L. Bailer-Jones et al. 2021) implies that, even at its faintest, BG CMi was $M_V \sim 6$. We therefore do not consider the WD to make a noticeable contribution to the optical flux, even in the low state.

From MJD $\sim 60751 - 60774$ (coincident with the light green portion of the optical light curve in Fig. 2), the optical flux of BG CMi increased, back towards its typical level. At this point in its evolution, the recovering optical flux implies that the disk was re-forming, and thus $\dot{M}_2 > \dot{M}_{\text{WD}}$. It was during this epoch that the *XMM-Newton* observations of BG CMi took place. Our (X-ray) spectral and (multi-wavelength) timing analysis indicates that accretion on to the WD was occurring via disk-overflow. The disk, though in the process of recovering, was still lower-mass than during the typical high state, and thus was less effective at absorbing X-rays. S. H. Lubow (1989) noted that the scale height of the ballistic stream from the companion on to the disk is typically bigger than that of the disk by a factor of 2–3. Overflowing material can then pass over the disk before being reincorporated into the rest of the disk (see also P. J. Armitage & M. Livio 1996, 1998, for example). We suggest here that the disk in BG CMi was

small enough that overflowing material was able to pass completely over the disk and reach the magnetospheric radius, R_{mag} , where it then flowed along the field lines on to the WD. This is similar to what was seen during the low state of V515 And, which went through a disk-overflow phase, before switching to stream-only accretion after the disk had fully emptied (A. E. Covington et al. 2022).

After the optical flux of BG CMi had recovered to its normal high state value (the dark green portion of the optical light curve in Fig. 2), we see the optical periodogram return to spin-dominated, much like it was prior to the low state. We interpret this as returning to a disk-fed accretion mode.

5. CONCLUSIONS

We have presented a multi-wavelength observing campaign of the 2025 low state of the IP BG CMi. Optical monitoring of the source show that its flux dropped by ~ 0.5 mag for ~ 50 d. We interpret this as being due to the mass transfer rate from the companion on to the disk, \dot{M}_2 , decreasing to a point where it was less than the rate at which mass was transferred from the disk on to the WD ($\dot{M}_2 < \dot{M}_{\text{WD}}$). This caused the disk to empty out over the course of the low state, though we cannot be certain that the disk ever completely dissipated. X-ray observations close to the end of the low state reveal a spectrum with significantly lower absorption than archival *Suzaku* observations of the source, which we interpret as the disk being lower mass than typical, and thus being a less-effective absorber of X-rays in our line of sight. We also find strong evidence for disk-overflow accretion during this portion of the low state, something which has been seen in numerous other IPs during their low states (see e.g. M. R. Kennedy et al. 2017; C. Littlefield et al. 2020; A. E. Covington et al. 2022). However, we do not find strong evidence for a complete switch to a stream-fed accretion mode.

We still do not have strong, testable theories for why \dot{M}_2 occasionally decreases in IPs, leading to low states. Recent studies of the other class of magnetic CVs, polars, have revealed evidence of a magnetic valve regulating mass transfer and thus controlling the high-low state cycle (P. A. Mason et al. 2022, 2024), but the magnetic fields of the WDs in IPs are significantly weaker and thus not expected to influence mass transfer at L_1 . M. Livio & J. E. Pringle (1994) proposed that starspots on the companion passing in front of the L_1 point are the cause of the observed drop in the optical flux of VY Scl stars, and thus, such a mechanism could theoretically be extended to IPs. A. Bianchini (1990) suggested that late-type donors in CVs can exhibit fractional variations

in stellar radius. Any variation in donor radius could potentially affect \dot{M}_2 due to the Roche Lobe overflow nature of IPs. However, it remains to be seen whether any, or none, of the above scenarios are responsible for the low states in IPs.

ACKNOWLEDGMENTS

AWS would like to thank Professor Ed Cackett for contributing observations to the BG CMi campaign with the Dan Zowada Memorial Observatory. We acknowledge with thanks the variable star observations from the AAVSO International Database contributed by observers worldwide and used in this research. We thank Norbert Schartel and the *XMM-Newton* OTAC chair for granting ToO observations of BG CMi at short notice. This work made use of Astropy³⁶ a community-

developed core Python package and an ecosystem of tools and resources for astronomy ([Astropy Collaboration et al. 2013, 2018, 2022](#)). This research made use of `ccdproc`, an Astropy package for image reduction ([M. Craig et al. 2017](#)). This work was supported by Slovak Research and Development Agency under contract No. APVV-20-0148. This article is based on observations made with the IAC80 telescope operated on the island of Tenerife by the Instituto de Astrofísica de Canarias in the Spanish Observatorio del Teide. COH is supported by NSERC Discovery Grant RGPIN-2023-04264, and Alberta Innovates Advance Program 242506334. CGN was supported by the Butler Summer Institute.

Facilities: XMM, Suzaku, Swift, OT:0.8m, Elizabeth, Csere, ING:Kapteyn, Great Basin, AAVSO

REFERENCES

Armitage, P. J., & Livio, M. 1996, *ApJ*, 470, 1024, doi: [10.1086/177928](https://doi.org/10.1086/177928)

Armitage, P. J., & Livio, M. 1998, *ApJ*, 493, 898, doi: [10.1086/305149](https://doi.org/10.1086/305149)

Astropy Collaboration, Robitaille, T. P., Tollerud, E. J., et al. 2013, *A&A*, 558, A33, doi: [10.1051/0004-6361/201322068](https://doi.org/10.1051/0004-6361/201322068)

Astropy Collaboration, Price-Whelan, A. M., Sipőcz, B. M., et al. 2018, *AJ*, 156, 123, doi: [10.3847/1538-3881/aabc4f](https://doi.org/10.3847/1538-3881/aabc4f)

Astropy Collaboration, Price-Whelan, A. M., Lim, P. L., et al. 2022, *ApJ*, 935, 167, doi: [10.3847/1538-4357/ac7c74](https://doi.org/10.3847/1538-4357/ac7c74)

Bailer-Jones, C. A. L., Rybizki, J., Fouesneau, M., Demleitner, M., & Andrae, R. 2021, *AJ*, 161, 147, doi: [10.3847/1538-3881/abd806](https://doi.org/10.3847/1538-3881/abd806)

Bianchini, A. 1990, *AJ*, 99, 1941, doi: [10.1086/115476](https://doi.org/10.1086/115476)

Bonneradeau, M. 2016, *Information Bulletin on Variable Stars*, 6168, 1, doi: [10.48550/arXiv.2011.04982](https://doi.org/10.48550/arXiv.2011.04982)

Bradley, L., Sipőcz, B., Robitaille, T., et al. 2025, `astropy/photutils`: 2.2.0, 2.2.0 Zenodo, doi: [10.5281/zenodo.1488940](https://doi.org/10.5281/zenodo.1488940)

Bruch, A. 2025, *ApJS*, 279, 48, doi: [10.3847/1538-4365/addir41](https://doi.org/10.3847/1538-4365/addir41)

Buckley, D. A. H., Haberl, F., Motch, C., et al. 1997, *MNRAS*, 287, 117, doi: [10.1093/mnras/287.1.117](https://doi.org/10.1093/mnras/287.1.117)

Buckley, D. A. H., Sekiguchi, K., Motch, C., et al. 1995, *MNRAS*, 275, 1028, doi: [10.1093/mnras/275.4.1028](https://doi.org/10.1093/mnras/275.4.1028)

Burrows, D. N., Hill, J. E., Nousek, J. A., et al. 2005, *SSRv*, 120, 165, doi: [10.1007/s11214-005-5097-2](https://doi.org/10.1007/s11214-005-5097-2)

Chambers, K. C., Magnier, E. A., Metcalfe, N., et al. 2016, arXiv e-prints, arXiv:1612.05560, <https://arxiv.org/abs/1612.05560>

Covington, A. E., Shaw, A. W., Mukai, K., et al. 2022, arXiv e-prints, arXiv:2202.08365, <https://arxiv.org/abs/2202.08365>

Craig, M., Crawford, S., Seifert, M., et al. 2017, `astropy/ccdproc`: v1.3.0.post1, v1.3.0.post1 Zenodo, doi: [10.5281/zenodo.1069648](https://doi.org/10.5281/zenodo.1069648)

de Martino, D., Mouchet, M., Bonnet-Bidaud, J. M., et al. 1995, *A&A*, 298, 849

den Herder, J. W., Brinkman, A. C., Kahn, S. M., et al. 2001, *A&A*, 365, L7, doi: [10.1051/0004-6361:20000058](https://doi.org/10.1051/0004-6361:20000058)

Done, C., & Magdziarz, P. 1998, *MNRAS*, 298, 737, doi: [10.1046/j.1365-8711.1998.01636.x](https://doi.org/10.1046/j.1365-8711.1998.01636.x)

Evans, P. A., Hellier, C., Ramsay, G., & Cropper, M. 2004, *MNRAS*, 349, 715, doi: [10.1111/j.1365-2966.2004.07542.x](https://doi.org/10.1111/j.1365-2966.2004.07542.x)

Ezuka, H., & Ishida, M. 1999, *ApJS*, 120, 277, doi: [10.1086/313181](https://doi.org/10.1086/313181)

Ferrario, L., de Martino, D., & Gänsicke, B. T. 2015, *SSRv*, 191, 111, doi: [10.1007/s11214-015-0152-0](https://doi.org/10.1007/s11214-015-0152-0)

Ferrario, L., Wickramasinghe, D., & Kawka, A. 2020, *Advances in Space Research*, 66, 1025, doi: [10.1016/j.asr.2019.11.012](https://doi.org/10.1016/j.asr.2019.11.012)

Ferrario, L., & Wickramasinghe, D. T. 1999, *MNRAS*, 309, 517, doi: [10.1046/j.1365-8711.1999.02860.x](https://doi.org/10.1046/j.1365-8711.1999.02860.x)

Garnavich, P., & Szkody, P. 1988, *PASP*, 100, 1522, doi: [10.1086/132358](https://doi.org/10.1086/132358)

Ginsburg, A., Sipőcz, B. M., Brasseur, C. E., et al. 2019, *AJ*, 157, 98, doi: [10.3847/1538-3881/aafc33](https://doi.org/10.3847/1538-3881/aafc33)

³⁶ <http://www.astropy.org>

Hellier, C. 1993, MNRAS, 265, L35, doi: [10.1093/mnras/265.1.L35](https://doi.org/10.1093/mnras/265.1.L35)

Hellier, C. 1997, MNRAS, 288, 817, doi: [10.1093/mnras/288.4.817](https://doi.org/10.1093/mnras/288.4.817)

Hellier, C., & Beardmore, A. P. 2002, MNRAS, 331, 407, doi: [10.1046/j.1365-8711.2002.05199.x](https://doi.org/10.1046/j.1365-8711.2002.05199.x)

Henden, A. A., & Honeycutt, R. K. 1995, PASP, 107, 324, doi: [10.1086/133557](https://doi.org/10.1086/133557)

HI4PI Collaboration, Ben Bekhti, N., Flöer, L., et al. 2016, A&A, 594, A116, doi: [10.1051/0004-6361/201629178](https://doi.org/10.1051/0004-6361/201629178)

Hill, K. L., Littlefield, C., Garnavich, P., et al. 2022, AJ, 163, 246, doi: [10.3847/1538-3881/ac5a51](https://doi.org/10.3847/1538-3881/ac5a51)

Ishisaki, Y., Maeda, Y., Fujimoto, R., et al. 2007, PASJ, 59, S113, doi: [10.1093/pasj/59.sp1.S113](https://doi.org/10.1093/pasj/59.sp1.S113)

Islam, N., & Mukai, K. 2021, ApJ, 919, 90, doi: [10.3847/1538-4357/ac134e](https://doi.org/10.3847/1538-4357/ac134e)

Jordi, K., Grebel, E. K., & Ammon, K. 2006, A&A, 460, 339, doi: [10.1051/0004-6361:20066082](https://doi.org/10.1051/0004-6361:20066082)

Joshi, A., Pandey, J. C., & Singh, H. P. 2019, AJ, 158, 11, doi: [10.3847/1538-3881/ab1ea6](https://doi.org/10.3847/1538-3881/ab1ea6)

Keel, W. C., Oswalt, T., Mack, P., et al. 2017, PASP, 129, 015002, doi: [10.1088/1538-3873/129/971/015002](https://doi.org/10.1088/1538-3873/129/971/015002)

Kennedy, M. R., Garnavich, P. M., Littlefield, C., et al. 2017, MNRAS, 469, 956, doi: [10.1093/mnras/stx880](https://doi.org/10.1093/mnras/stx880)

Kim, Y. G., Andronov, I. L., Park, S. S., & Jeon, Y. B. 2005, A&A, 441, 663, doi: [10.1051/0004-6361:20052995](https://doi.org/10.1051/0004-6361:20052995)

King, A. R., & Lasota, J.-P. 1991, ApJ, 378, 674, doi: [10.1086/170467](https://doi.org/10.1086/170467)

Knigge, C., Baraffe, I., & Patterson, J. 2011, ApJS, 194, 28, doi: [10.1088/0067-0049/194/2/28](https://doi.org/10.1088/0067-0049/194/2/28)

Langford, A., Littlefield, C., Garnavich, P., et al. 2022, AJ, 163, 4, doi: [10.3847/1538-3881/ac3010](https://doi.org/10.3847/1538-3881/ac3010)

Littlefield, C., Bonnardeau, M., & Garnavich, P. 2025, The Astronomer's Telegram, 17050, 1

Littlefield, C., Garnavich, P., Kennedy, M. R., et al. 2020, ApJ, 896, 116, doi: [10.3847/1538-4357/ab9197](https://doi.org/10.3847/1538-4357/ab9197)

Livio, M., & Pringle, J. E. 1994, ApJ, 427, 956, doi: [10.1086/174202](https://doi.org/10.1086/174202)

Lomb, N. R. 1976, Ap&SS, 39, 447, doi: [10.1007/BF00648343](https://doi.org/10.1007/BF00648343)

Lubow, S. H. 1989, ApJ, 340, 1064, doi: [10.1086/167458](https://doi.org/10.1086/167458)

Magnier, E. A., Schlafly, E. F., Finkbeiner, D. P., et al. 2020, The Astrophysical Journal Supplement Series, 251, 6, doi: [10.3847/1538-4365/abb82a](https://doi.org/10.3847/1538-4365/abb82a)

Mason, K. O., Breeveld, A., Much, R., et al. 2001, A&A, 365, L36, doi: [10.1051/0004-6361:20000044](https://doi.org/10.1051/0004-6361:20000044)

Mason, P. A., Littlefield, C., Monroy, L. C., et al. 2022, ApJ, 938, 142, doi: [10.3847/1538-4357/ac91cf](https://doi.org/10.3847/1538-4357/ac91cf)

Mason, P. A., Hakala, P., Wu, K., et al. 2024, ApJ, 965, 96, doi: [10.3847/1538-4357/ad27d7](https://doi.org/10.3847/1538-4357/ad27d7)

McHardy, I. M., Pye, J. P., Fairall, A. P., et al. 1982, IAUC, 3687, 1

McHardy, I. M., Pye, J. P., Fairall, A. P., et al. 1984, MNRAS, 210, 663, doi: [10.1093/mnras/210.3.663](https://doi.org/10.1093/mnras/210.3.663)

Mitsuda, K., Bautz, M., Inoue, H., et al. 2007, PASJ, 59, 1, doi: [10.1093/pasj/59.sp1.S1](https://doi.org/10.1093/pasj/59.sp1.S1)

Mukai, K. 2017, PASP, 129, 062001, doi: [10.1088/1538-3873/aa6736](https://doi.org/10.1088/1538-3873/aa6736)

Mukai, K., Kinkhabwala, A., Peterson, J. R., Kahn, S. M., & Paerels, F. 2003, ApJ, 586, L77, doi: [10.1086/374583](https://doi.org/10.1086/374583)

Mukai, K., Rana, V., Bernardini, F., & de Martino, D. 2015, ApJL, 807, L30, doi: [10.1088/2041-8205/807/2/L30](https://doi.org/10.1088/2041-8205/807/2/L30)

Murray, J. R., Armitage, P. J., Ferrario, L., & Wickramasinghe, D. T. 1999, MNRAS, 302, 189, doi: [10.1046/j.1365-8711.1999.02110.x](https://doi.org/10.1046/j.1365-8711.1999.02110.x)

Mushotzky, R. F., & Szymkowiak, A. E. 1988, in NATO Advanced Science Institutes (ASI) Series C, Vol. 229, NATO Advanced Science Institutes (ASI) Series C, ed. A. C. Fabian, 53–62

Parker, T. L., Norton, A. J., & Mukai, K. 2005, A&A, 439, 213, doi: [10.1051/0004-6361:20052887](https://doi.org/10.1051/0004-6361:20052887)

Patterson, J. 1994, PASP, 106, 209, doi: [10.1086/133375](https://doi.org/10.1086/133375)

Patterson, J., de Miguel, E., Kemp, J., et al. 2020, ApJ, 897, 70, doi: [10.3847/1538-4357/ab863d](https://doi.org/10.3847/1538-4357/ab863d)

Scargle, J. D. 1982, ApJ, 263, 835, doi: [10.1086/160554](https://doi.org/10.1086/160554)

Shaw, A. W., & Heinke, C. O. 2025, The Astronomer's Telegram, 17089, 1

Shaw, A. W., Miller, J. M., Grinberg, V., et al. 2022, MNRAS, 516, 124, doi: [10.1093/mnras/stac2213](https://doi.org/10.1093/mnras/stac2213)

Strüder, L., Briel, U., Dennerl, K., et al. 2001, A&A, 365, L18, doi: [10.1051/0004-6361:20000066](https://doi.org/10.1051/0004-6361:20000066)

Suleimanov, V., Revnivtsev, M., & Ritter, H. 2005, A&A, 435, 191, doi: [10.1051/0004-6361:20041283](https://doi.org/10.1051/0004-6361:20041283)

Suleimanov, V. F., Doroshenko, V., & Werner, K. 2019, MNRAS, 482, 3622, doi: [10.1093/mnras/sty2952](https://doi.org/10.1093/mnras/sty2952)

Tanaka, Y., Inoue, H., & Holt, S. S. 1994, PASJ, 46, L37

Tremblay, P.-E., Bergeron, P., & Gianninas, A. 2011, ApJ, 730, 128, doi: [10.1088/0004-637X/730/2/128](https://doi.org/10.1088/0004-637X/730/2/128)

Turner, M. J. L., Abbey, A., Arnaud, M., et al. 2001, A&A, 365, L27, doi: [10.1051/0004-6361:20000087](https://doi.org/10.1051/0004-6361:20000087)

Verner, D. A., Ferland, G. J., Korista, K. T., & Yakovlev, D. G. 1996, ApJ, 465, 487, doi: [10.1086/177435](https://doi.org/10.1086/177435)

Warner, B. 1986, MNRAS, 219, 347, doi: [10.1093/mnras/219.2.347](https://doi.org/10.1093/mnras/219.2.347)

Wilms, J., Allen, A., & McCray, R. 2000, ApJ, 542, 914, doi: [10.1086/317016](https://doi.org/10.1086/317016)

Wynn, G. A., & King, A. R. 1992, MNRAS, 255, 83, doi: [10.1093/mnras/255.1.83](https://doi.org/10.1093/mnras/255.1.83)

Yuasa, T., Nakazawa, K., Makishima, K., et al. 2010, A&A, 520, A25, doi: [10.1051/0004-6361/201014542](https://doi.org/10.1051/0004-6361/201014542)